Alloying effect of PdCu-TiO$_2$ in photocatalytic membrane reactor for efficient removal of humic acid foulant

Haibo Yin [a,1], Junyang Zhang [a,b,1], Yunlong Wang [c,1], Xiaoguang Zhao [c], Yakun Qu [c], Yue Peng [a], Hexing Li [b], Yuning Huo [b,*], Junhua Li [a,*]

[a] State Key Joint Laboratory of Environment Simulation and Pollution Control, School of Environment, Tsinghua University, Beijing 100084, PR China
[b] The Education Ministry Key Lab of Resource Chemistry, Joint International Research Laboratory of Resource Chemistry, Ministry of Education, Shanghai Key Laboratory of Rare Earth Functional Materials, Shanghai Frontiers Science Research Base of Biomimetic Catalysis, and College of Chemistry and Materials Science, Shanghai Normal University, Shanghai 200234, PR China
[c] Sinopec Research Institute of Petroleum Processing Co., Ltd, Beijing 100083, PR China

ARTICLE INFO

ABSTRACT

Photocatalytic membrane reactor (PMR), coupling photocatalysis and membrane separation, has shown a considerable potential in foulant removal. However, the serious membrane fouling and fragile membrane stability still limit the application of current PMR systems. Here, we report a strategy that PdCu alloy deposited on TiO$_2$, which is incorporated with polyvinylidene fluoride membrane, achieves high humic acid (HA) rejection efficiency (100%) with enhanced membrane permeation and anti-fouling performance. Detailed characterizations demonstrate that alloying effect of PdCu-TiO$_2$ plays multiple roles in improving PMR performance: (1) providing the paired Pd-Cu sites for enhancing HA adsorption and transferring electrons from Pd-Cu sites to HA to improve photocatalytic HA removal; (2) inducing the photothermal effect due to the carrier damping, which directly enhances membrane permeation. The remarkable properties of PdCu-TiO$_2$ membrane in PMR confirm the significance of alloying effect for treating aqueous organic pollutants.

1. Introduction

Natural organic matter (NOM) existing ubiquitously in natural waters has been considered as one of the major foulants [1–3]. Humic acid (HA), which constitutes a vast majority of NOM, has been considered to react with the major disinfectants used in water treatment to produce a host of disinfection byproducts (DBPs) [4–6]. The removal of HA is important in meeting the stringent DBPs regulations and providing safe drinking water [7,8]. Due to the resistance to biodegradation, various physical/chemical technologies have been offered to remove HA from water, such as coagulation, electrocoagulation, adsorption, ion exchange, and membrane processes [9–12]. Among them, membrane technology has been considered as a well-established method in HA removal due to its high stability and efficiency [10,13]. However, a major challenge in membrane separation processes is membrane fouling problem, where HA accumulates on the surface or interior of membrane, leading to a flux decline [14,15]. Therefore, it is of great significance to improve the permeation and anti-fouling performance of membranes for the practical HA treatment [15–17].

Compared with other membrane fouling control technologies, photocatalytic technology, as one kind of advanced oxidation processes, can effectively solve the filtering membrane fouling problems [18–20]. Immobilizing photocatalysts in the membrane structure with nanoscale-confined spaces can constitute a more effective catalytic system for foulant removal [21,22]. From the perspective of energy savings and environmental protection, photocatalysis coupling membrane separation for HA removal driven by renewable solar energy will undoubtedly receive more attention. Recently photocatalytic membrane reactor (PMR) system has been gradually developed for organic foulants removal [23,24]. Thereinto, the development of highly efficient photocatalysts is the most important point of PMR systems. In light of the remarkable advantages of TiO$_2$ in photocatalysis, TiO$_2$-based photocatalytic membranes have been studied to achieve high foulants removal and improve anti-fouling performance of membrane [21,25,26]. However, most of them in PMR system still face the dilemma of low photoconversion efficiency and low fouling resistance of membrane [18,19].

Compared to a single metal, alloys play a more crucial role in transferring photo-generated electrons and thus inhibiting electron-hole recombination [27,28]. Meanwhile, considering the unique geometry configuration and electronic interactions of alloys, the strategy of alloy modification to semiconductors has been widely applied in photocatalysis [29–31]. Among alloys, PdCu alloy nanoparticles (NPs) with the prominent synergistic effect between metal atoms have attracted extensive attention as excellent cocatalyst in photocatalytic redox reactions, such as the oxidation of benzene series and the conversion of CO_2 [32–36]. For example, it has been widely recognized that Cu can provide active sites for photocatalytic CO_2 conversion but suffer from oxidation and the side reaction of H_2 evolution [36]. The paired Pd-Cu by alloying Pd with Cu can apparently improve the resistance of Cu to oxidation and suppress H_2 production [35]. Therefore, the introduction of PdCu alloy in PMR system is expected to effectively remove HA, thereby improving the fouling resistance of membrane. In addition, the choice of membrane materials is also critical in PMR system [37–39]. Compared with other membrane materials, polyvinylidene fluoride (PVDF) has been regarded as a desirable membrane material owing to its good mechanical strength, low cost, and easy corporation with photocatalysts [40,41]. However, it still can not well solve the limited water permeation problem in existing PMR system [41]. The damping resonances during carriers transfer process, which are induced by plasmonic resonance effect, can cause apparent photothermal effect of PdCu alloy [42]. The increased temperature by converting photon energy into local heat in photocatalysis process can effectively promote water evaporation and further improve water permeation performance [43–48]. Based on these advantages, PdCu alloy coupled TiO_2 (PdCu-TiO_2) can be an ideal photocatalyst for developing PMR system with both enhanced foulants removal, anti-fouling, and permeation properties of membrane.

In this work, we design and prepare PdCu-TiO_2 hybrids via a solution-processed impregnation-H_2 reduction method. The PMR system is constructed by blending PdCu-TiO_2 into PVDF membrane via phase inversion method. The new PMR system achieves up to 100% rejection efficiency of HA and enhances anti-fouling performance of membrane in photocatalytic process. Notably, the strong photothermal effect induced by alloying effect of PdCu-TiO_2/PVDF can simultaneously heat the feed solution and partially vaporize water to accelerate permeation efficiency. Furthermore, the density functional theory (DFT) calculations demonstrate that highly dispersed PdCu alloys are the key factor for facilitating photocatalytic removal of HA.

2. Experimental section

2.1. Chemicals and materials

Polyvinylidene fluoride (PVDF, FR904) was provided from Shanghai 3 F New Materials Co., Ltd, N, N-dimethylformamide (DMF), Polyvinylpyrrolidone (PVP) and Copper (II) chloride dihydrate ($CuCl_2 \cdot 2H_2O$) were purchased from Aladdin Chemical Co., Ltd, Hydrochloric acid (HCl), Sodium hydroxide (NaOH), Potassium chloropalladite (K_2PdCl_4), Titanium dioxide (TiO_2, P25), Ascorbic acid (AA) and Potassium bromide (KBr) were purchased from Shanghai Macklin Biochemical Co., Ltd, Humic acid (HA) was obtained from Sigma-Aldrich, Deionized water was used in all of the experiments.

2.2. Synthesis of PdCu-TiO_2 hybrids

PdCu-TiO_2 hybrids were prepared by a solution-processed impregnation-H_2 reduction method (Scheme S1). Firstly, 1000 mg of P25 TiO_2 was dispersed in 50 mL deionized water under ultrasound at room temperature for 20 min. Then 525 mg of polyvinylpyrrolidone (PVP, Mw = 55,000), 600 mg of ascorbic acid (AA), and 1200 mg of KBr were added into the suspension under magnetic stirring in an oil bath at 80 °C for 5 min, respectively. Subsequently, certain amounts of K_2PdCl_4 and $CuCl_2 \cdot 2H_2O$ solutions were added to the suspension. The reaction

suspension was heated at 80 °C in air for 180 min. The molar ratio of Pd to Cu was 5: 1, and the total metal content was kept at 1.0 mmol. The sample was washed with water and ethanol several times to remove AA and PVP by centrifugation, and then vacuum dried at 80 °C for 12 h. In the final step, H_2 reduction was carried out at 300 °C. The obtained sample is denoted as PdCu-TiO_2 (or named Pd_5Cu_1-TiO_2). For comparison, certain amounts of K_2PdCl_4 (0.750 and 0.875 mmol) and $CuCl_2 \cdot 2H_2O$ (0.250 and 0.125 mmol) solutions were mixed and injected into the suspension in the same manner, the obtained samples were denoted as Pd_3Cu_1-TiO_2 and Pd_7Cu_1-TiO_2, respectively. In addition, Pd-TiO_2 and Cu-TiO_2 hybrids were also prepared by the above method without adding $CuCl_2 \cdot 2H_2O$ or K_2PdCl_4, respectively.

2.3. Preparation of PdCu-TiO_2/PVDF photocatalytic membrane

PdCu-TiO_2/PVDF photocatalytic membranes were fabricated by phase conversion method (Scheme S2). The photocatalyst can be uniformly distributed in membrane structures via phase conversion method. As shown, PdCu-TiO_2 hybrids (2.0 wt%) were dispersed in N,N-Dimethylformamide (DMF) solution (80 wt%) under sonication for 30 min. Then the mixture was physically stirred in an oil bath at 80 °C, PVP (Mw = 8000, 3.0 wt%) and PVDF powder (15 wt%) were sequentially added into the mixture. After stirring for 12 h, the membrane casting solution was kept in vacuum oven at 80 °C to remove the air bubbles. The as-prepared casting solution was poured onto the automatic coating machine (SANNO 6000) and scraped with the gap to casting knife of 250 μm at the speed of 10 cm/sec. The composite membrane was then immersed in deionized water bath at 25 °C for 10 min to accomplish the phase-inversion process. The obtained membrane is denoted as PdCu-TiO_2/PVDF (or named P-PCT-2), where 2 represents the amount (wt%) of PdCu-TiO_2 hybrids blended in membrane casting solution. For comparison, Pd-TiO_2/PVDF, Cu-TiO_2/PVDF and TiO_2/PVDF membranes were prepared as the above process with blending Pd-TiO_2, Cu-TiO_2, and TiO_2 membrane casting solution, respectively. In addition, PdCu-TiO_2/PVDF membranes with different blending amount were also prepared by blending certain amounts of optimized PdCu-TiO_2 hybrids (1.0, 3.0, and 4.0 wt%) in membrane casting solution. The obtained membrane is denoted as P-PCT-*X* (PVDF-PdCu-TiO_2-*X*), where *X* represents the amount (wt%) of PdCu-TiO_2 hybrids blended in membrane casting solution.

2.4. Preparation of HA feed solution

The humic acid was pretreated before used in order to remove impurities (fulvic acids, metals, and ash). Firstly, 4 g humic acid was dispersed in 40 mL HCl solution (0.1 mol/L), the suspension was stirred for 2 h, and centrifuged at 10,000 rpm for 10 min. After the centrifugation, the precipitate was re-dispersed in HCl solution. The procedure was repeated five times. Next, the precipitate was dissolved in 40 mL NaOH solution (0.1 mol/L). Then, the solution was adjusted to ca. pH 7.0 with HCl, then stirred for 2 h, and centrifuged at 10,000 rpm for 10 min. The supernatant was filtered twice through 0.45 μm PVDF filters and diluted with DI water. After pre-treatment, the solution was diluted, and its concentration were measured using Total Organics (TOC) analyzer. Finally, 10 mg/L feed solution was configured and further prepared according to the measured concentration.

2.5. HA removal and permeation test in PMR system

A laboratory-built photocatalytic membrane separation reactor system (Scheme 1) was used to investigate HA removal and permeability of photocatalytic membranes. The membrane cell contained a quartz glass in the top part of the cell to allow the transmission of light onto an effective membrane area of 28.26 cm^2. One Xenon lamp with full wavelength (CHF-XM500, light intensity = 3.89 kWm^{-2}) was positioned with the distance of 8.0 cm above the quartz window. The filtration
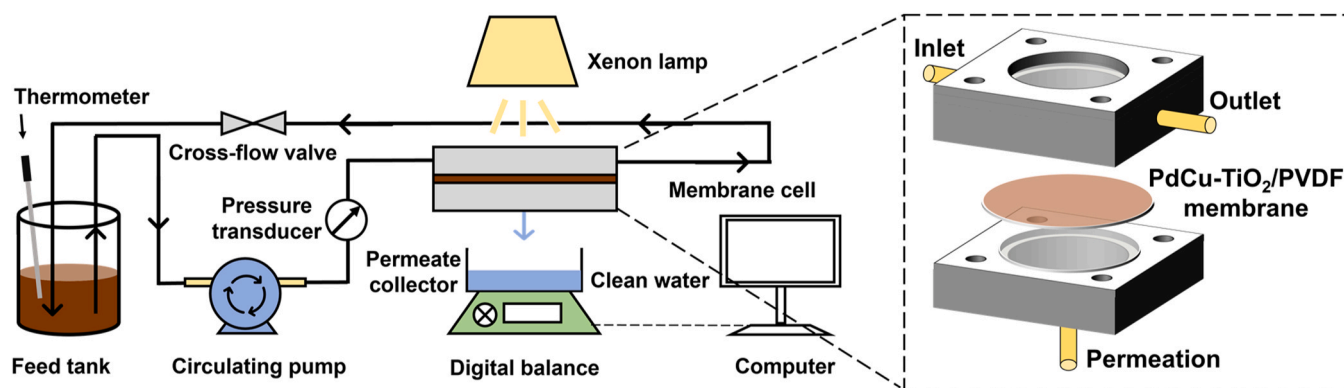
Scheme 1. Illustration of the laboratory-built photocatalytic membrane separation reactor system.

transmembrane pressure was supported from circulating pump (EC-101, e-chen). The permeation solution was collected and weighed with a time interval of 15 min on a digital balance (OHAUS SPX2201ZH), which is connected to the computer for data collection. A temperature probe (Kechuangjin DS18B20) was placed in the feed tank to record the temperature change of feed solution in real time. Reaction conditions: membrane diameter = 6.0 cm, 2 L 10 mg/L HA solution, pre-press pressure = 1 bar, transmembrane pressure = 0.5 bar, time of filtration = 360 min. For HA photocatalytic degradation reaction: 20 mg photocatalyst, 100 mL 10 mg/L HA solution, adsorption time = 30 min (in dark), irradiation time = 60 min

The permeation and removal performances of membranes were evaluated by this PMR system. Before test, the membrane was pre-pressed with deionized water at 1.0 bar for 30 min. Then, the pure water flux measurement was operated at 0.5 bar with deionized water for 30 min. The permeation flux was recorded and calculated according to Eq. 1 (Eq. 1).

$$J = \frac{V}{A \cdot T} \tag{1}$$

Where J represented the flux ($L \cdot m^{-2} \cdot h^{-1} \cdot bar^{-1}$), V was the water permeation volume (L), A was the effective membrane filtration area (m^2), T was the filtration time (h).

For HA removal test, 2.0 L HA solution (10 mg/L) was prepared in feed tank and light irradiation was turned on. The membrane filtration was continued for 360 min and the HA removal efficiency was calculated according to Eq. 2.

$$R = \left(1 - \frac{C}{C_0}\right) \times 100\% \tag{2}$$

Where C and C_0 were the TOC concentration of feed and the permeated HA solution, respectively, which were tested by TOC analyzer (VARIO TOC cube).

2.6. Photocatalytic degradation of HA

The photocatalytic activities of photocatalysts were reflected by the degradation of HA under light irradiation. 20 mg of each photocatalyst were suspended into 100 mL HA solutions (10 mg/L). The distance between the reaction vessel and Xenon lamp was set at approximately 8 cm and the mixture was magnetically stirred for efficient photocatalyst suspending. Then the photocatalytic degradation was initiated as the light turned on. After 60 min's irradiation, the mixture was centrifuged for analysis, and the removal efficiency was defined according to Eq. 3:

$$Degradation \quad efficiency = \left(1 - \frac{C_1}{C_0}\right) \times 100\% \tag{3}$$

Where C_0 and C_1 were the TOC concentration of initial HA solution and

photodegraded HA solution, which were tested by TOC analyzer (VARIO TOC cube).

2.7. Detection of degradation products of HA under light irradiation

The detection of degradation products of HA was conducted by a photocatalytic reactor (CEL-HPR1001 +, CEAULIGHT). In the reactor, a small quartz beaker had a height of 10 cm and a diameter of 5 cm, where the photocatalysts (20 mg) were suspended in 50 mL HA solution (10 mg/L). A 300 W Xe lamp was used as the light source and positioned above the reactor 8 cm. The photocatalytic reaction was typically performed for 60 min after bubbling with Ar gas for 30 min. The production of CO_2 in gas phase was determined by a GC, the products of product in liquid phase were determined by LC-MS.

2.8. Photothermal water evaporation performance

The photothermal-water evaporation performance was measured on various membranes in a petri dish. The composite membrane with area of 28.26 cm^2 was floated in 30 mL HA solution (10 mg/L). The Xenon lamps was located at 8 cm above the membrane surface. The photothermal-water evaporation measurement was continued for 60 min. And an infrared thermal imager camera (FLIR A300) was employed to measure and record the temperature change of membrane surface. The water evaporation property of membranes was evaluated by monitoring the loss weight of HA solution on the digital balance, and the water evaporation rate (v, $kg \cdot m^{-2} \cdot h^{-1}$) was calculated according to Eq. 4.

$$v = \frac{dm}{S dt} \tag{4}$$

Where m was the mass of evaporated solution (kg), S was the surface area of membrane (m^2) and t was the evaporation time (h).

2.9. Material characterization

XRD measurements were recorded using a BRUKER D8/Advance X-ray diffractometer (Cu Kα X-ray: λ = 0.1545 nm). The scanning electron microscopy (SEM) images were taken on a ZEISS GEMINISEM 500 electron field emission microscope. The surface morphology and roughness were characterized by Atomic Force Microscope (AFM, Bruker MultiMode 8.0) in contact mode with a scanning range of 2.0 × 2.0 μm and scanning frequency of 0.99 Hz. Transmission electron microscopy (TEM) and energy-dispersive spectroscopy (EDS) measurements were performed on a JEOL JEM 2100 microscope with an accelerating voltage of 200 kV. The functional groups were detected by FT-IR (INNOVA-1412i) in the wavenumber range of 500–2000 cm^{-1}. X-ray photoelectron spectroscopy (XPS) and Auger electron spectroscopy measurements were carried out using an ESCALab250XI photoelectron

spectrometer. All binding energies were referenced to the C 1 s peak at 284.8 eV. The pore size distribution and specific surface area were calculated according to Barrett-Joyner-Halenda (BJH) and Brunauer-Emmett-Teller (BET) methods based on N_2 adsorption isotherms measured at $-196\ ^{\circ}C$ on MicrotracBEL Corp. Samples were degassed under vacuum at 200 °C for 4 h prior to data collection. Raman spectroscopy was tested on Confocal Raman microscope under an excitation of 532 nm laser light. Pd K-edge and Cu K-edge XAFS measurements were performed on the beamline BL01C1 in NSRRC. The radiation was monochromatized by a Si (111) double-crystal monochromator. UV/Vis-NIR diffuse reflectance spectra were measured on Lambda 900 from PerkinElmer UV WinLab. The degradation products of HA were analyzed using gas chromatography (GC, 7890 A, Agilent) and liquid chromatograph-mass spectrometer (LC-MS, UPLC, Thermo). Photocurrent response, impedance curves, and Mott-Schottky curves were measured by CHI-760E from Shanghai CHENHUA by using platinum foil, and Ag/AgCl (saturated KCl solution) were employed as the counter, and reference electrodes, respectively. ESR spectra were performed on A300–10/12 from Bruker in Germany. Water contact angle were measured on a contact angle measuring system (JC 2000D 3 POWEREACH) using a deionized water droplet of 2.0 *u*L as an indicator.

2.10. DFT calculation detail

The Vienna ab initio simulation package (VASP, version 5.4.4) was utilized to calculate the properties of catalysts. All the model structures were optimized by using the Perdew-Burke-Ernzerhof (PBE) form of the generalized gradient approximation (GGA), with a 400 eV of kinetic cutoff energy. A [3 × 3] supercell and four Pd, Cu, and Pd-Cu (111) atomic layers was used for the plane-wave expansion of the electronic wave function, respectively, of which two bottom layers were fixed to their bulk positions during the geometry optimizations. Thereinto, the atomic ratio of Pd to Cu was close to that of ICP results. The slab models of the support TiO_2 for above nanoparticles were constructed. These slab models were separated by a 15 Å vacuum combined with a $3 \times 3 \times 1$ Gamma-Pack k-point mesh due to the large crystal cell (~18 Å × 18 Å) of slab model. Moreover, all slab models were relaxed until the SCF tolerance was below 10^{-6} eV and atomic forces were below 0.05 eV/Å.

3. Results and Discussion

3.1. The structural characterization of PdCu-TiO$_2$ hybrids

PdCu-TiO$_2$ hybrids composing of PdCu alloy NPs on TiO$_2$ were prepared by solution-processed impregnation-H_2 reduction method (Scheme S1). PdCu alloy NPs with a face-centered cubic (fcc) phase are in situ grown on TiO$_2$ (Fig. 1a-b and Fig. S1), where the atomic ratios of Pd to Cu can be controlled by adjusting the concentrations of Pd and Cu precursors (Inductively coupled plasma-optical emission spectroscopy (ICP-OES), Table S1). Atomic-resolution high-angle annular dark-field scanning transmission electron microscope (HAADF-STEM) image of PdCu-TiO$_2$ (Fig. 1a) clearly indicates spheric PdCu alloy NPs with a mean size of 4.5 nm (inserted in Fig. 1a) are uniformly dispersed on TiO$_2$, which is totally different from Pd-TiO$_2$ with the cubic structures of Pd NPs (mean size of 6.5 nm, Fig. S2). Notably, no Cu NPs are found in Cu-TiO$_2$ hybrids (Fig. S3), which is because Cu species cannot be loaded on TiO$_2$ alone without assistance of Pd species.[36,49,50] Fig. 1b displays that PdCu alloy has the lattice spacing of 2.2 Å, which corresponds
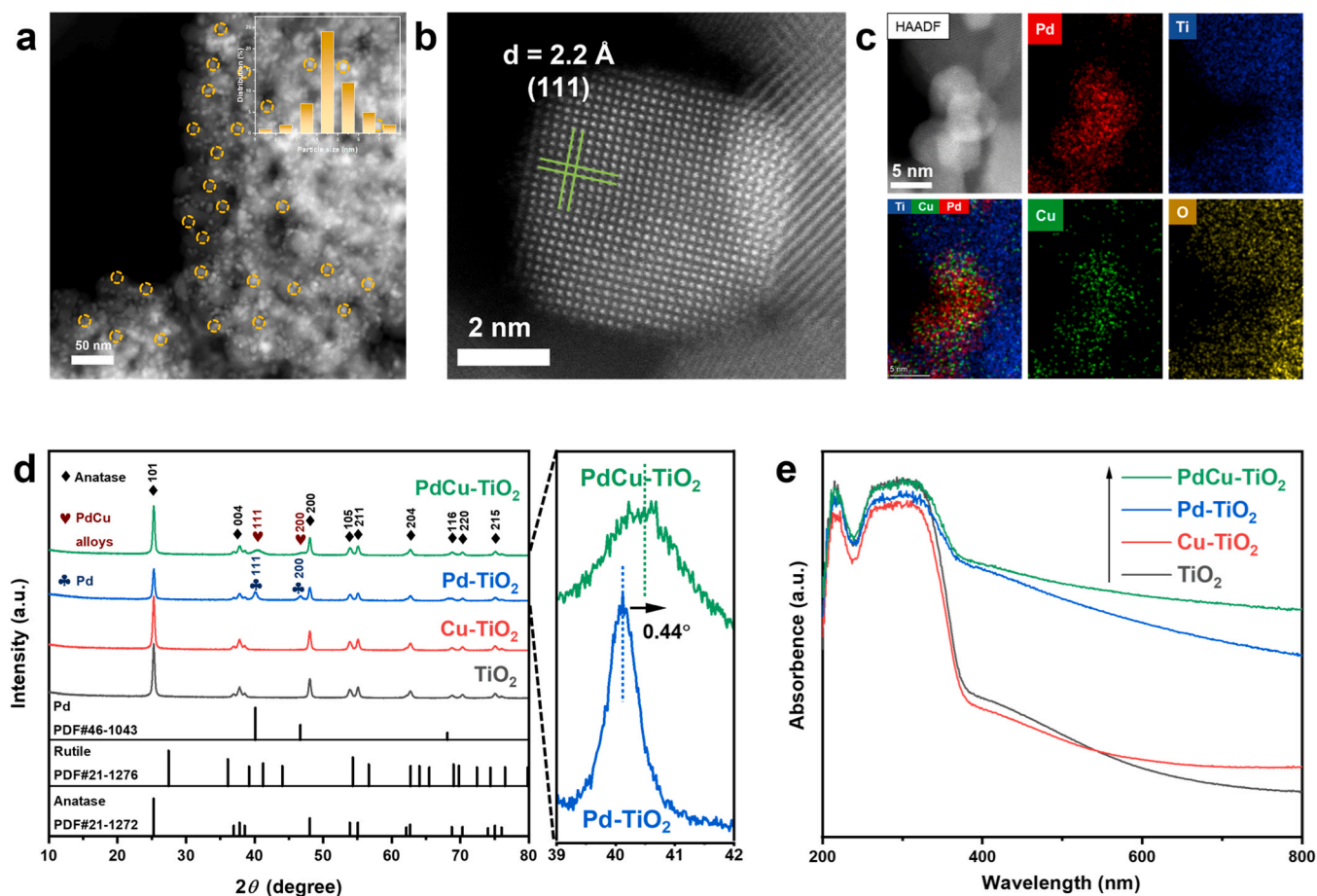

Fig. 1. (a) HAADF-STEM images and (b) high-resolution HAADF-STEM image of PdCu-TiO$_2$ hybrids. (c) Corresponding EDS elemental mapping images of PdCu-TiO$_2$ hybrids. (d) XRD patterns, (e) UV-Vis adsorption spectra of PdCu-TiO$_2$, Pd-TiO$_2$, Cu-TiO$_2$ hybrids and TiO$_2$.

to the (111) plane of fcc PdCu alloy (Fig. S1c). Compared to Pd-TiO$_2$ with lattice spacing of 2.4 Å (Fig. S2b), the reduced 0.2 Å in PdCu alloy can be ascribed to the incorporation of Cu species into Pd lattice.[36] Meanwhile, energy-dispersive spectroscopy (EDS) mapping from both HAADF-STEM (Fig. 1c) and TEM (Fig. S4) further reveals the spatial distribution of Pd, Cu, Ti and O elements and confirms the uniformly distribution of PdCu NPs on TiO$_2$. And same peak locations of Pd and Cu elements in the corresponding EDS elemental line scan (Fig. S4a-b) confirm that highly dispersed Pd species tightly chelate with Cu species, highlighting the formation of highly dispersed PdCu alloy NPs. Furthermore, X-ray diffraction (XRD) pattern (Fig. 1d) of PdCu-TiO$_2$ hybrids shows a distinct anatase phase (PDF#21–1272) of TiO$_2$. Meanwhile, the characteristic diffraction peak ($2\theta = 40.5°$) corresponds to PdCu alloy NPs with a dominantly exposed (111) facet. The apparent peak shift ($2\theta = 0.44°$, enlarged Fig. 1d) caused by the incorporation of Cu species confirms the formation of alloy compared to peak of Pd NPs in Pd-TiO$_2$ (PDF#46–1043). Similar phenomena are found in Pd$_3$Cu$_1$-TiO$_2$ and Pd$_7$Cu$_1$-TiO$_2$ hybrids (Fig. S5), which also indicates the formation of PdCu alloy on TiO$_2$. Raman spectra of PdCu-TiO$_2$, Pd-TiO$_2$ and Cu-TiO$_2$ show typical characteristic vibrations (E$_{g1}$, B$_{1g}$, A$_{1g}$, and E$_{g2}$) of TiO$_2$ (Fig. S6), suggesting TiO$_2$ remains good structure stability even after the deposition of PdCu alloy or Pd NPs. N$_2$ isothermal adsorption/desorption measurements (Fig. S7) indicate that PdCu-TiO$_2$, Pd-TiO$_2$, Cu-TiO$_2$ and TiO$_2$ possess similar mesoporous structures with surface area (~ 56.42 m^2 g^{-1}), pore volume (~ 0.29 cm^3 g^{-1}), and average pore sizes of ~ 20.46 nm (Table S2). This proves that the introduction of PdCu or Pd NPs does not affect the textural properties of TiO$_2$ during preparation process. The optical property of PdCu-TiO$_2$ is also studied by UV-Vis spectra (Fig. 1e). Among PdCu-TiO$_2$ hybrids with different molar ratios of Pd and Cu, Pd$_5$Cu$_1$-TiO$_2$ (PdCu-TiO$_2$) achieves the strongest visible light absorption (Fig. S8). Compared with Pd-TiO$_2$, Cu-TiO$_2$, and TiO$_2$, PdCu-TiO$_2$ hybrids show stronger visible light absorption, which is mainly induced by the surface plasmon resonance effect[42] of PdCu alloy NPs and more oxygen vacancies (Fig. S9).

3.2. Structural parameters and coordination environment of PdCu-TiO$_2$ hybrids

X-ray photoelectron spectroscopy (XPS) measurements are performed to elucidate the oxidation states of Pd and Cu elements. XPS spectra of PdCu-TiO$_2$ hybrids confirm the presence of Pd and Cu species (Fig. S10a). For Pd 3d spectra of PdCu-TiO$_2$ hybrids (Fig. S10d), two peaks with binding energies (BEs) at 339.4 and 334.1 eV are attributed to the 3d$_{3/2}$ and 3d$_{5/2}$ peaks of Pd^0,[36] respectively. Notably, compared
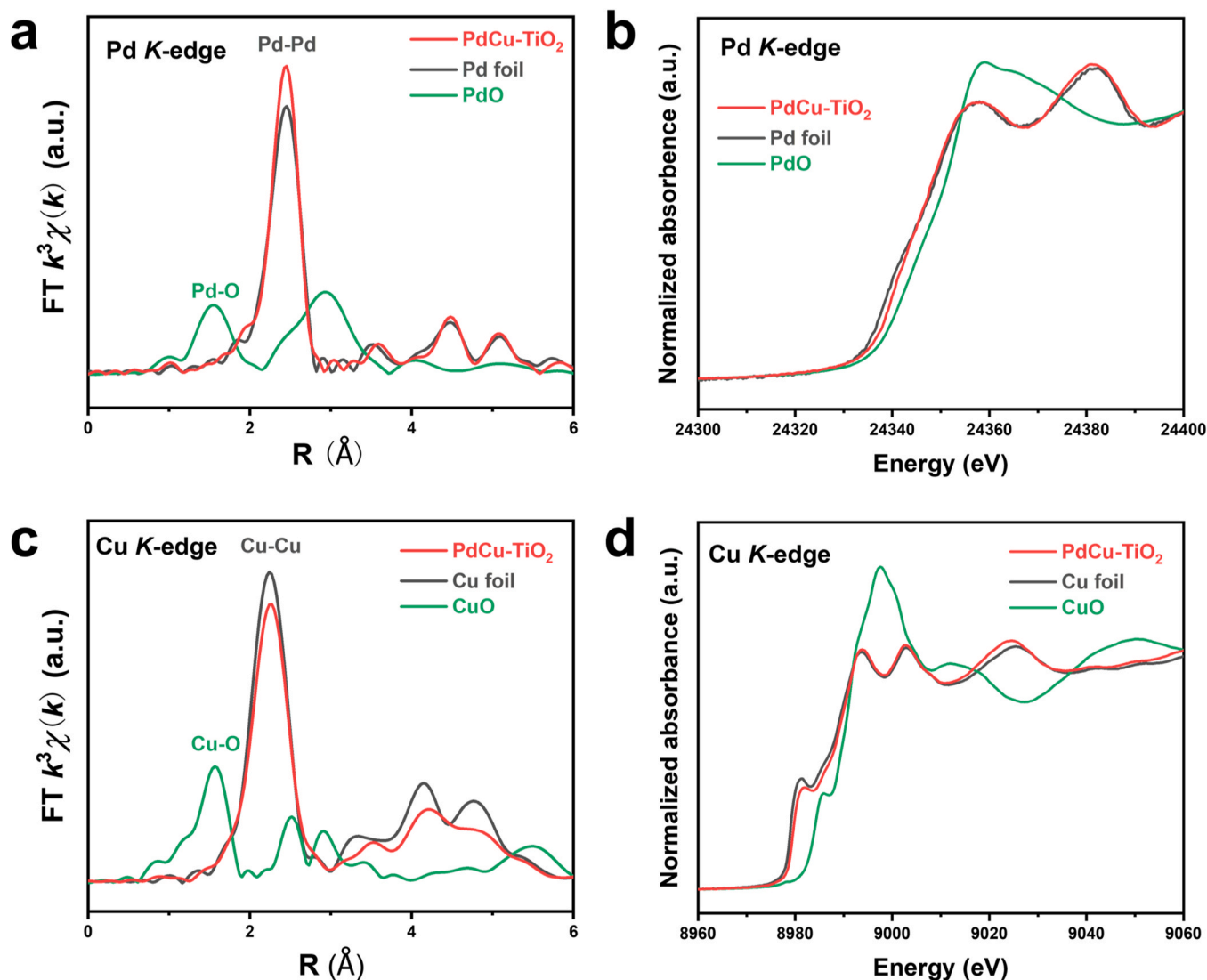

Fig. 2. (a) Pd K-edge FT k^3-weighted $\chi(k)$-function of the EXAFS and (b) XANES spectra of PdCu-TiO$_2$, Pd foil and PdO. (c) Cu K-edge FT k^3-weighted $\chi(k)$-function of the EXAFS and (d) XANES spectra of PdCu-TiO$_2$, Cu foil and CuO.

to Pd-TiO$_2$, the positive shift of Pd BEs peaks in PdCu-TiO$_2$ indicates the electron interaction between Pd and Cu in PdCu alloy (Fig. S10d). The BEs of Cu 2p at 930.6 and 951.0 eV are assigned to Cu 2p$_{3/2}$ and Cu 2p$_{1/2}$ of Cu^0 or Cu$^+$ species in PdCu-TiO$_2$ (Fig. S10e). On the contrary, based on XPS, XRD (Fig. 1d), and ICP-OES (Table S1) analysis, only small amounts of Cu species can be deposited on TiO$_2$ without the assistance of Pd species. In addition, by adjusting the Pd/Cu molar ratio, the oxidation states of Pd and Cu (Fig. S11d-e) of Pd$_3$Cu$_1$-TiO$_2$ and Pd$_7$Cu$_1$-TiO$_2$ hybrids are consistent with that of Pd$_5$Cu$_1$-TiO$_2$ hybrids. Furthermore, X-ray absorption fine structure (XAFS) measurements are performed to precisely reveal the local structural information of Pd and Cu elements. The Pd K-edge Fourier-transformed extended X-ray absorption fine structure (FT-EXAFS) spectra of PdCu-TiO$_2$ hybrids present Pd-Pd coordination at 2.45 Å similar to that of Pd foil (Fig. 2a). Moreover, Pd K-edge X-ray absorption near edge structure (XANES) curves of PdCu-TiO$_2$ hybrids also show similar curve trend to that of Pd foil rather than that of PdO, indicating the valence of Pd species in PdCu-TiO$_2$ is Pd^0 (Fig. 2b). Meanwhile, Cu K-edge FT-EXAFS spectra (Fig. 2c) and XANES spectra (Fig. 2d) of PdCu-TiO$_2$ hybrids have no apparent difference from that of Cu foil, where Cu-Cu bonds locate at 2.26 Å, indicating Cu^0 in hybrids are the only form of Cu species in PdCu-TiO$_2$ hybrids. Furthermore, wavelet transform X-ray absorption fine structure (WT-EXAFS) is performed to correlate the FT-EXAFS peaks with R- and k- spaces. Based on the similar feature of Pd foil (Fig. S12a), the WT intensity maximum (2.45 Å) at Pd K-edge of PdCu-TiO$_2$ hybrids mainly stems from the Pd-Pd coordination (Fig. S12b), which is completely different from PdO (Fig. S12c). Meanwhile, the WT intensity (2.26 Å) at Cu K-edge of PdCu-TiO$_2$ hybrids apparently corresponds to that of Cu foil rather than CuO (Fig. S12d-f). The above analysis further proves that Pd and Cu species in PdCu-TiO$_2$ hybrids exist in the form of Pd^0 and Cu^0, respectively. Furthermore, according to EXAFS curve fitting (Fig. S13 **and** Fig. S14), the metal-metal bond lengths and metal coordination numbers (Table 1) are extracted for investigating bonding information. The Pd or Cu metal atoms in the fcc lattice are known to perfectly have the coordination number of 12.[36] Based on the fitting results, although Pd and Cu atoms in PdCu alloy mainly exist in the form of Pd-Pd and Cu-Cu coordination, respectively, part of Cu atoms is coordinated to two Pd atoms (Table 1) to construct Pd-Cu coordination, further highlighting the formation of PdCu alloy.

3.3. Photo-electrochemistry characterization of PdCu-TiO$_2$ hybrids

Photo-electrochemistry and electrochemical impedance measurements are operated to study the dynamics of photo-generated carriers (Fig. S15a-b). Compared to Pd-TiO$_2$, Cu-TiO$_2$ and TiO$_2$, PdCu-TiO$_2$ hybrids exhibit the highest photocurrent density (Fig. S15a), indicating PdCu alloy can efficiently separate photo-generated electron-hole pairs. Moreover, PdCu-TiO$_2$ hybrids show the smallest semicircle diameter than Pd-TiO$_2$, Cu-TiO$_2$ and TiO$_2$ according to the Nyquist plots of electrochemical impedance spectra (EIS) (Fig. S15b), demonstrating PdCu alloy can reduce the resistance by increasing charge transfer ability. The Mott-Schottky spectra was used for analyzing the flat band potential

(E$_{fb}$) under light irradiation (Fig. S16). The E$_{fb}$ values calculated from the intercept of the axis with potential values are − 0.92, − 0.64, − 0.51, and − 0.68 V vs Ag/AgCl for PdCu-TiO$_2$, Pd-TiO$_2$, Cu-TiO$_2$ and TiO$_2$, respectively. Furthermore, based on the valence band XPS (VB-XPS) spectra (Fig. S15c), the valence bands of TiO$_2$ and PdCu-TiO$_2$ hybrids are 4.28 and 3.47 eV, respectively. The bandgap value of PdCu-TiO$_2$ (2.42 eV) has 0.71 eV less than that of TiO$_2$ (3.13 eV), highlighting PdCu alloy can promote the excitation of TiO$_2$ under light irradiation (Fig. S15d). By the meticulous analysis of photo-generated carriers transfer and electronic band structure, the diagram of band energies of PdCu-TiO$_2$ hybrids and TiO$_2$ are calculated (Fig. S15e). With the assistance of Schottky junction, the essential role of PdCu alloy is to reduce the bandgap of TiO$_2$ by enhancing the valence band and facilitate electrons transfer, thereby improving the photocatalytic performance.

3.4. The structural characterization of PdCu-TiO$_2$/PVDF membrane

PdCu-TiO$_2$/PVDF photocatalytic membrane is fabricated via phase conversion method (Scheme S2). XRD patterns (Fig. 3a) indicate the successful incorporation of photocatalysts and membrane. And the characteristic peaks intensities of PdCu-TiO$_2$ of PdCu-TiO$_2$/PVDF membranes is gradually enhanced with the increase of blending amount (Fig. S17). In addition, Fourier transform infrared (FT-IR) spectra show the introduction of photocatalysts do not change the surface functional groups (e.g. C═O, CF$_2$ and CH$_2$) of PVDF membrane (Fig. S18). From UV-Vis spectra (Fig. 3b), PVDF shows no light response from UV to visible light range because of the nature of insulator. After incorporating photocatalysts into PVDF membrane, the light absorptions of photocatalyst/PVDF membranes show significantly enhancement. Notably, the trends of light absorption enhancement among TiO$_2$/PVDF, Cu-TiO$_2$/PVDF, Pd-TiO$_2$/PVDF and PdCu-TiO$_2$/PVDF membranes are corresponding well with those of TiO$_2$, Cu-TiO$_2$, Pd-TiO$_2$ and PdCu-TiO$_2$ (Fig. 1e), indicating the optical properties of photocatalysts can be effectively maintained even in membranes. Furthermore, this light adsorption intensity correlates well with increasing amount of PdCu-TiO$_2$ in PVDF membranes (Fig. S19). Meanwhile, atomic force microscope (AFM) is performed to study the surface roughness of membranes (Fig. S20). The decreased roughness can effectively reduce the contact area between the membrane and foulants, leading to good anti-fouling performance.[51] Pure water flux is an important indicator for evaluating the performance of membranes in application, which can be affected by factors such as membrane roughness and hydrophilicity. Compared with the original PVDF membrane (13.51 L/m^2·h·bar), pure water flux largely increases to 21.99 L/m^2·h·bar with the incorporation of PdCu-TiO$_2$ (Fig. 3c). Depend on the smoother surface and stronger hydrophilicity, PdCu-TiO$_2$/PVDF membrane achieves the largest pure water flux (Fig. 3c and Fig. S21), which lays a good foundation for the subsequent treatment of HA solution. As shown in Fig. 3d, compared with PVDF membrane, PdCu-TiO$_2$/PVDF membrane with suitable photocatalyst blending amount (Fig. S22) shows smoother surface due to well dispersion of PdCu-TiO$_2$, where PdCu-TiO$_2$/PVDF with PdCu-TiO$_2$ blending amount of 2% shows minimal average roughness. The morphologies of PVDF and PdCu-TiO$_2$/PVDF membranes are observed by scanning electron microscope (SEM, Fig. 3e-i). Compared with PVDF (Fig. 3e and f), PdCu-TiO$_2$ hybrids are mainly deposited in the pore channels of membrane while only small part is fixed onto the surface of membrane (Fig. 3g-i). EDS mapping images of cross-section further prove the uniform distribution of Pd, Cu and Ti elements in PdCu-TiO$_2$/PVDF membrane (Fig. 3j). The size dispersion of TiO$_2$, Cu-TiO$_2$, Pd-TiO$_2$ and PdCu-TiO$_2$ particles in the membranes were evaluated by SEM (Fig. S23), the photocatalysts are uniformly dispersed into the membrane structure, most of the photocatalysts blended in all membranes are immobilized with the size of 1.0 μm. In addition, the surface hydrophilicity properties of different membranes are evaluated by water contact angle measurements (Fig. S24 and Fig. S25). The contact angle of PdCu-TiO$_2$/PVDF membranes has decreased with the increasing

Table 1
Structural parameters of PdCu-TiO$_2$, Pd foil, and Cu foil extracted from the EXAFS fitting.

Sample	EXAFS	Bond	CN[a]	R (Å)[b]	σ^2 (10^{-3} Å^2)[c]
PdCu-TiO$_2$	Pd K	Pd-Pd	10.4	2.75	6.1
		Pd-Cu	1.3	2.64	1.3
	Cu K	Cu-Cu	9.8	2.58	12.3
		Cu-Pd	2.0	2.65	5.0
Pd foil	Pd K	Pd-Pd	12	2.74	5.6
Cu foil	Cu K	Cu-Cu	12	2.54	8.8

[a] CN, coordination number.
[b] R, the distance to the neighboring atom.
[c] σ^2, the mean square relative displacement (MSRD).
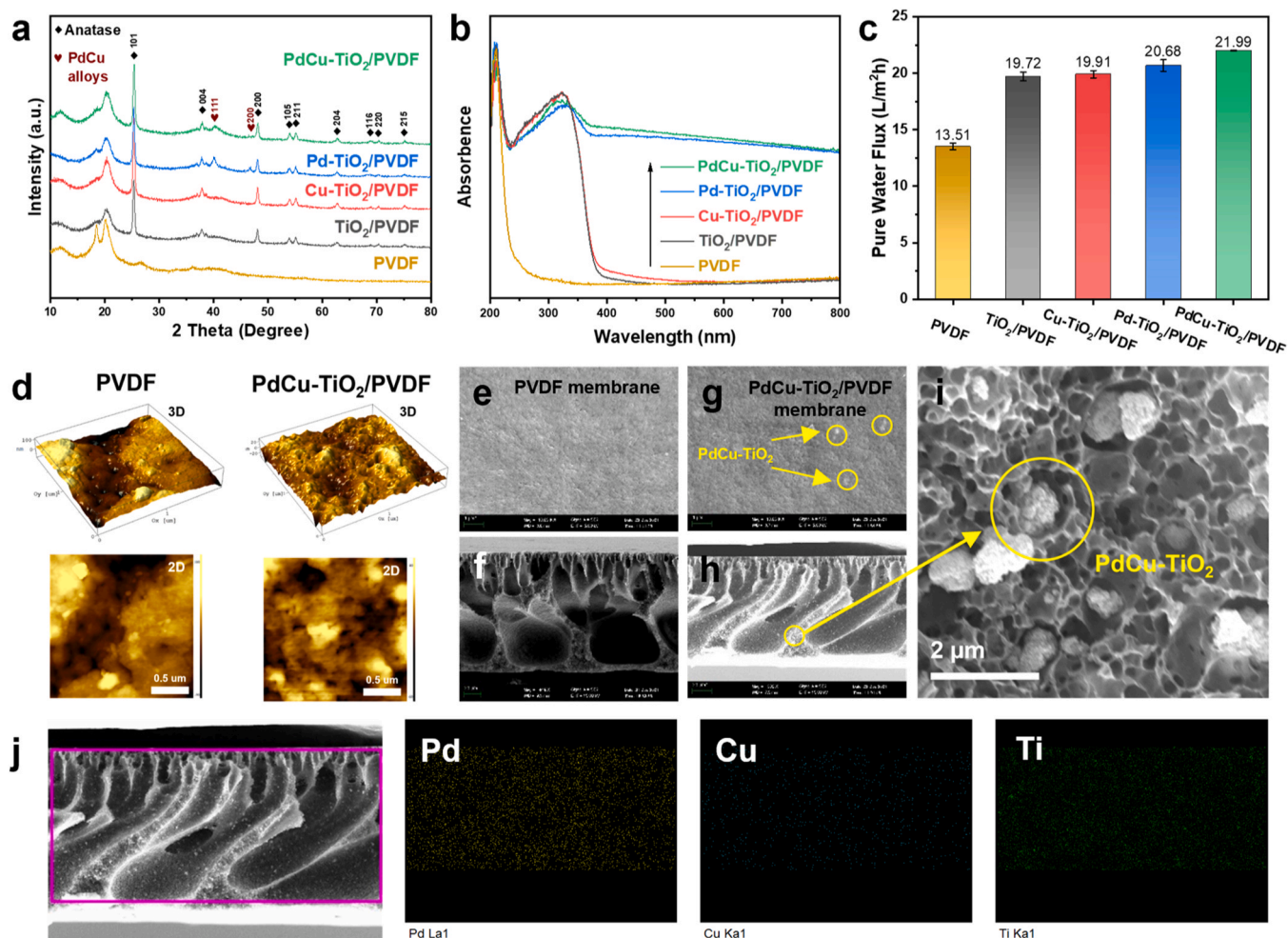
Fig. 3. (a) XRD patterns and (b) UV-Vis adsorption spectra of PdCu-TiO$_2$/PVDF, Pd-TiO$_2$/PVDF, Cu-TiO$_2$/PVDF, TiO$_2$/PVDF and PVDF membranes. (c) Pure water fluxes of PdCu-TiO$_2$/PVDF, Pd-TiO$_2$/PVDF, Cu-TiO$_2$/PVDF, TiO$_2$/PVDF and PVDF membranes. (d) 3D and 2D AFM images of PdCu-TiO$_2$/PVDF and PVDF membranes. SEM images of (e) surface and (f) cross-section of PVDF membrane, and (g) surface and (h) cross-section of PdCu-TiO$_2$/PVDF membrane with (i) enlarged SEM image. (j) EDS mapping images of cross-section with distribution of Pd, Cu and Ti elements in PdCu-TiO$_2$/PVDF membrane.

PdCu-TiO$_2$ blending amount (Fig. S25). Compared with PVDF, the hydrophilicities of photocatalysts/PVDF promote obviously due to the decreased contact angles. The enhanced hydrophilicity is mainly attributed to the hydrophilic nature of TiO$_2$.

3.5. Performance of HA removal in PMR system

The continuous removal of HA is achieved by ultrafiltration in a laboratory-built PMR system (Scheme 1 and Scheme S3). The operational performance of PMRs can be evaluated from HA rejection efficiency (from the aspect of permeace solution), anti-fouling performance (from the aspect of membrane) and the total removal efficiency (from the aspect of feed solution). As shown in Fig. 4a, the HA rejection efficiency of PVDF membrane is 85.7% under light irradiation. After incorporating TiO$_2$-based photocatalysts (TiO$_2$, Cu-TiO$_2$, Pd-TiO$_2$ and PdCu-TiO$_2$) with PVDF membranes, photocatalysts embedded in the pore channels of membrane can apparently enhance the HA adsorption rates (Fig. S26), so PMR system can effectively improve the rejection efficiency of HA, achieving up to 100%. Furthermore, the relative water flux curve profiles during the filtration under light irradiation is presented in Fig. 4b, which is calculated by the ratio of real-time HA flux (J_{HA}) to pure water flux (J_{water}, Fig. S27). After filtration of 360 min, PVDF membrane shows a significant flux decline (63%) in permeation because of severe membrane fouling. After incorporating photocatalysts, the fluxes of these PMR systems show more stable water flux.

Indeed, with TiO$_2$/PVDF an increase of the flux of 29.5% observed, whereas it was 73.3% and 46.8% for Pd-TiO$_2$/PVDF and Cu-TiO$_2$/PVDF, respectively, indicating the introduction of Pd or Cu improves the anti-fouling performance of membranes to some extent. This is mainly because Pd NPs or Cu NPs facilitate the transfer of photo-generated electrons and holes by Schottky junction (Fig. S16) and avoiding their recombination. Water flux of PdCu-TiO$_2$/PVDF system keeps very stable during the filtration process and only 6% of flux decline is observed after 6 h's filtration, which is much lower than Pd-TiO$_2$/PVDF and Cu-TiO$_2$/PVDF systems due to the synergistic effect of Pd and Cu. At the same time, from the PMR point of view it is important to show the course of changes of HA concentration in feed and permeate in time of the process. Thus, as shown in Fig. 4c, the total removal efficiency is evaluated by comparing the concentration of initial HA and HA in the remaining feed solution after filtration, in which the PdCu-TiO$_2$/PVDF membrane achieves the highest total removal efficiency owing to the promoted photocatalytic performance by alloying effect. The membrane separation process includes the discharge of low concentration permeate and the gradual concentration of feed solution. The total removal efficiency of 45.74% achieved by PdCu-TiO$_2$/PVDF membrane indicates that the feed solution maintains the original HA concentration and does not gradually concentrate with the filtration process, which to some extent ensures the membrane's anti-fouling performance and long-term removal stability. The above analysis fully highlights the role of alloying effect in enhancing permeation, anti-fouling performance and HA removal
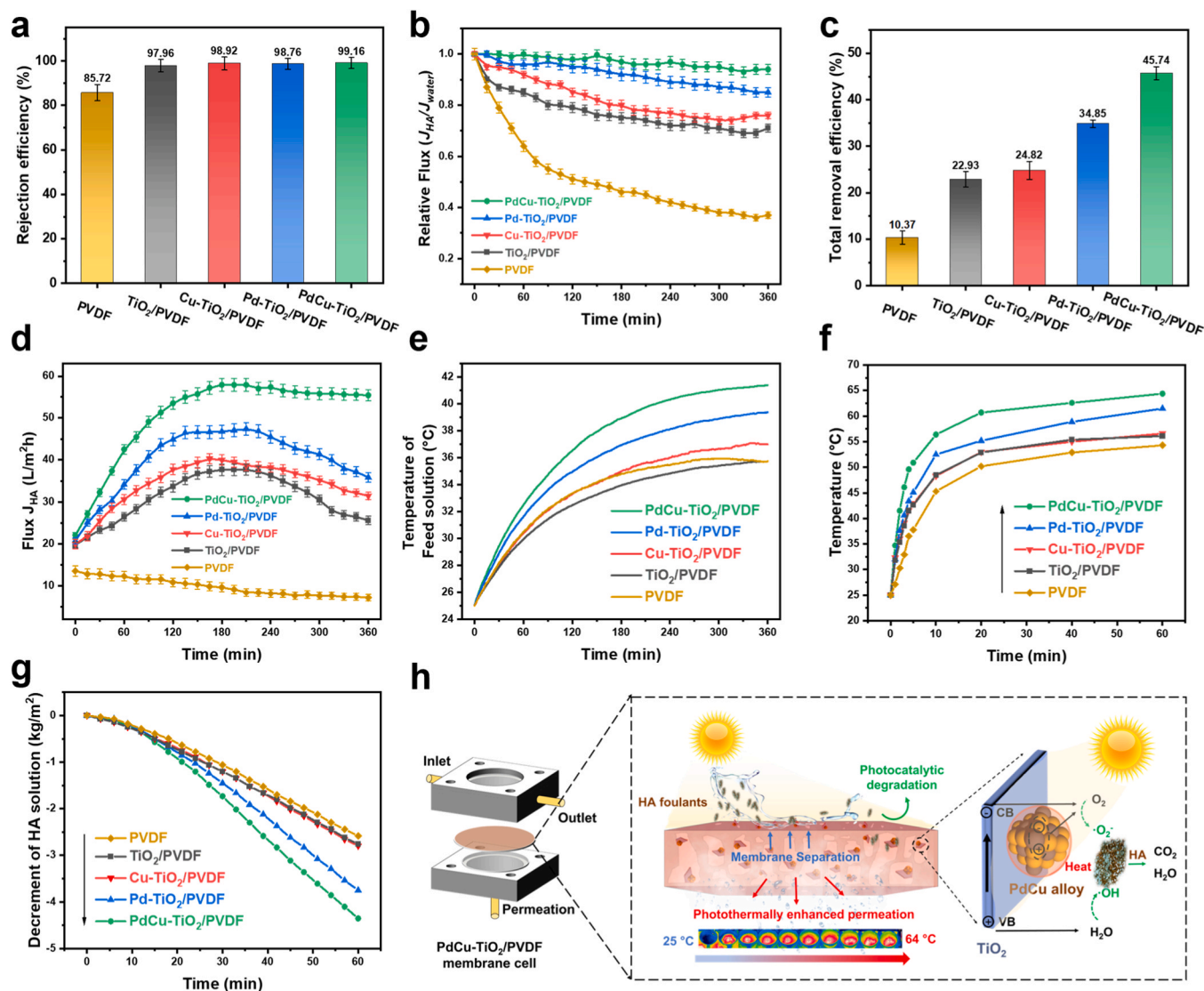
Fig. 4. (a) HA rejection efficiency, (b) the relative flux curve profiles, (c) the total removal efficiency, (d) the actual water fluxes, (e) the temperature changing curves of HA feed solution of PdCu-TiO$_2$/PVDF, Pd-TiO$_2$/PVDF, Cu-TiO$_2$/PVDF, TiO$_2$/PVDF and PVDF membranes during the filtration under light irradiation. (f) Surface temperature changes and (g) water mass changes of PdCu-TiO$_2$/PVDF, Pd-TiO$_2$/PVDF, Cu-TiO$_2$/PVDF, TiO$_2$/PVDF and PVDF membranes in photothermal water evaporation test. (h) Schematic illustration of PMR system based on PdCu-TiO$_2$/PVDF photocatalytic membrane for HA removal.

efficiency of membranes on PMR system. Besides, the overall performance of PMRs based on PdCu-TiO$_2$/PVDF membranes with different photocatalyst blending amount are also evaluated (Fig. S28). The PMR systems with lower amount blending of PdCu-TiO$_2$ (P-PCT-1) and higher amount blending of PdCu-TiO$_2$ (P-PCT-3, 4) show a certain degree of water flux decline compared with that of P-PCT-2 (Fig. S28a).

Furthermore, we study the essential reasons for the improvement of PMR system performance induced by alloying effect. Firstly, the molar ratio of Pd and Cu in Pd$_x$Cu$_1$-TiO$_2$ hybrids is optimized by HA degradation test (Fig. S29a). Among all photocatalysts, Pd$_5$Cu$_1$-TiO$_2$ (PdCu-TiO$_2$) hybrids achieve the highest performance with degradation efficiency of 100% under light irradiation without temperature control. At constant temperature (25 °C), the HA degradation efficiency of PdCu-TiO$_2$ (67.37%) is obviously higher than those of Pd-TiO$_2$ (52.35%), Cu-TiO$_2$ (37.52%) and TiO$_2$ (35.41%), highlighting the advantage of PdCu alloy than single metal in pure photocatalytic process (Fig. S29b). For HA degradation without temperature control in photocatalytic system, compared with the limited performance improvement of other photocatalysts, the degradation rate of PdCu-TiO$_2$ is obviously improved, reaching nearly 100%, indicating the stronger photothermal effect

induced by alloying effect under light irradiation (Table 2). That is, alloying effect plays an important in both improving photocatalytic performance and improving photothermal property. This photothermal property induced by alloying effect is further reflected when PdCu-TiO$_2$ is embedded in the PVDF membranes (Fig. 4d). Compared with other PMRs with only stable flux, the actual water flux of PdCu-TiO$_2$

Table 2
The photothermal property of PdCu-TiO$_2$, Pd-TiO$_2$, Cu-TiO$_2$ hybrids and TiO$_2$ in HA degradation experiment.

Sample	Initial temperature of solution before reaction	Temperature of solution after reaction
Pd$_3$Cu$_1$-TiO$_2$	25 °C	61.1 °C
Pd$_5$Cu$_1$-TiO$_2$	25 °C	63.5 °C
Pd$_7$Cu$_1$-TiO$_2$	25 °C	63.2 °C
Pd-TiO$_2$	25 °C	49.7 °C
Cu-TiO$_2$	25 °C	35.4 °C
TiO$_2$	25 °C	33.2 °C

incorporated PMR shows an upward and stable trend, which the photothermal effect induced by alloying effect of PdCu-TiO$_2$ contributes to the promoted permeance performance. The temperature rising of feed solution is continuously heated by PdCu-TiO$_2$/PVDF under light irradiation, compared with dark conditions (25 °C), the temperature of feed solution in PMR system rises to 40 °C (Fig. 4e), and its water flux increases significantly (151.9%) (Fig. 4d). The enhancement of water flux can be ascribed to the decrease of water viscosity and flow resistance owing to the enhanced temperature. The increase in kinetic energy of water molecules results in increasing the diffusion coefficient and reducing the intermolecular interaction, which elevates the diffusion rate and further facilitates water through the membrane. Additional filtration measurements were conducted on PdCu-TiO$_2$/PVDF membrane by using a series of HA solutions with different temperature, the results are further proved the effect of feed temperature to the flux of membranes (Fig. S30). Furthermore, the flux of PdCu-TiO$_2$/PVDF membrane under constant feed temperature is measured to shield the influence of feed temperature (Fig. S31). Interestingly, the flux under constant feed temperature is lower than rising temperature, but it still follows the trend which the water flux increases firstly and then stabilizes. Even under constant temperature conditions, PdCu-TiO$_2$/PVDF membrane still has a certain photothermal effect, the permeance water can be evaporated through the membrane by in situ heating of the immobilized PdCu-TiO$_2$ photocatalysts onto the pore structure channels. Additional experiments are carried out to evaluate the photothermal water evaporation performance (Fig. S32-34). PdCu-TiO$_2$/PVDF shows higher surface temperature increase (Fig. 4f and Fig. S33) and corresponding higher photothermal water evaporation performance (Fig. 4g) than Pd-TiO$_2$/PVDF, Cu-TiO$_2$/PVDF, TiO$_2$/PVDF and PVDF, which stems from the alloying effect. The increased temperature further leads to the heating of the feed solution (Fig. 4e) and in situ evaporation (Fig. S34c, e) of the permeation solution, which jointly promote the enhancement of the permeation flux. Meanwhile, the photothermally promoted permeance of PdCu-TiO$_2$/PVDF membranes with different photocatalyst blending amount are also evaluated (Fig. S34b, d, f and Fig. S35). The PMR systems with higher amount blending of PdCu-TiO$_2$ (P-PCT-2,3,4) show a certain degree of water flux improvement. Therefore, the enhanced photocatalytic performance and photothermal effect induced by alloying effect are the keys for PMR system to effectively remove HA, achieve strong anti-fouling and permeation performance of membrane under light irradiation (Fig. 4h).

According to the PdCu-TiO$_2$/PVDF membrane stability test (Fig. S36), the flux of each cycle remains the trend of increasing first and then stabilizing. The same initial flux in each cycle indicates the stably anti-fouling performance. Besides, the rejection efficiency (Fig. S36b), adsorption rate (Fig. S36c), and total removal efficiency (Fig. S36d) in each cycle also remain consistent. This suggests that PdCu-TiO$_2$/PVDF membrane is resistant to light radiation, the action of reactive oxygen species (ROS) and high temperature during long-term operation on the PMR. PdCu-TiO$_2$/PVDF membranes before and after test were also systematically characterized by SEM, XRD and FT-IR analysis (Fig. S37) to trace their changes in physicochemical properties. PdCu-TiO$_2$ is stably immobilized onto the structure of PVDF membrane (Fig. S37a-d). Meanwhile, the morphology of membrane keeps the original ordinary asymmetric structure of ultrafiltration membrane, which is divided into the thick porous support layer with fully developed macropores and a top dense skin layer (Fig. S37c-d). Furthermore, no obvious change is observed from XRD and FT-IR spectra of PdCu-TiO$_2$/PVDF membranes before and after test (Fig. S37e-f), indicating the stable physicochemical properties. Meanwhile, the evaluation of the practical separation properties of real water was also performed (Fig. S38). The real water was obtained from Huangpu River in Shanghai, China, followed by the pretreatment steps including sedimentation and microfiltration. The concentration of total organic carbon (TOC) in real water was measured at 7.86 mg/L by TOC analyzer (VARIO TOC cube). Comparing to the flux of PdCu-TiO$_2$/PVDF membrane filtered with laboratory self-prepared HA

solution without no salt species, the anti-fouling performance and rejection efficiency still maintain the same level with treating real water. This indicates that the elevated temperature (up to 40 °C) shows little influence on the crystallization of salts present in real water, suggesting no inactivation of the surface of the photocatalytic membrane. The permeated water after the filtration on PdCu-TiO$_2$/PVDF membrane is obviously cleaner than the real water before treatment, which is more expected to be applied for actual wastewater treatment.

3.6. HA removal mechanism with DFT calculations

Given this situation, we further explore the intrinsic reasons of PdCu alloy in PMR system for enhancing HA removal and membrane permeation performance. Considering that the enhancement of HA removal and anti-fouling performances of PdCu-TiO$_2$/PVDF membrane is mainly dominated by alloying effect during the filtration process, we investigate the radical species generated by photocatalysts under light irradiations. Based on the analysis of electron spin resonance (ESR) measurements, $\cdot$O$_2^-$ (Fig. 5a) and $\cdot$OH (Fig. 5b) are detected in all photocatalytic membranes. Compared to Pd-TiO$_2$/PVDF, Cu-TiO$_2$/PVDF, and TiO$_2$/PVDF, PdCu-TiO$_2$/PVDF generates more $\cdot$O$_2^-$ and $\cdot$OH under light irradiation due to the alloying effect, further suggesting that PdCu-TiO$_2$/PVDF has stronger HA removal ability in PMR system. In addition, similar ESR results are found for the corresponding photocatalysts (Fig. S39), and the quenching experiments also prove the importance of $\cdot$OH and $\cdot$O$_2^-$ radicals (Fig. S40).

Furthermore, the degradation products of HA by PdCu-TiO$_2$ hybrids under light irradiation are analyzed using gas chromatograph (GC) and liquid chromatograph-mass spectrometer (LC-MS, positive ion mode) to study the possible HA transformation pathways. From the GC spectrum (Fig. 5c), product CO$_2$ is detected, indicating that HA can be mineralized by photocatalysis. Meanwhile, from LC-MS spectrum (Fig. 5d), the intermediate byproducts contain 2-furoic acid, oxydimethanol, phenols, 2-(propylamino) ethanol, acetoacetic acid, phthalic acid, and 2-hydroxy-4-methylpentanoic acid (Table S3). Based on the detection of radial species and degradation products of HA removal process, we deduce the plausible photocatalytic HA removal pathways in membrane fouling alleviation process of PMR system (Fig. 5e). Thereinto, the alloying effect induced by PdCu alloy plays a key role in above system, which is further reflected in the following DFT calculation. Considering HA is a complex organic matter, the most representative structure (C$_9$H$_9$NO$_6$) of HA fragment is selected as the simulation unit.[4,11] As an important step for the whole reaction process, the initial adsorption of C$_9$H$_9$NO$_6$ molecules with PdCu-TiO$_2$ hybrids shows a marked difference compared with Pd-TiO$_2$ (−0.34 eV), Cu-TiO$_2$ (−0.3 eV), and TiO$_2$ (1.2 eV) (Fig. 5f), where PdCu-TiO$_2$ hybrids have the strongest C$_9$H$_9$NO$_6$ adsorption capacity owing to the lowest adsorption energy (−0.61 eV). The projected density of states (PDOS) is used to further illustrated the electronic band structure between the 3d orbitals of Pd and Cu of PdCu alloy active centers in PdCu-TiO$_2$ and the 2p orbits of O in the adsorbed C$_9$H$_9$NO$_6$ * (Fig. 5g-h). Compared with the overlap area between the Pd 3d-O 2p and Cu 3d-O 2p, the p-d orbital hybridizations between Pd or Cu atoms of the paired Pd-Cu sites and O atoms in C$_9$H$_9$NO$_6$* are obviously stronger than those of Pd-TiO$_2$ and Cu-TiO$_2$, which can effectively form the strong chemical bonds of Cu-O and Pd-O. More importantly, the charge density differences and the Bader charge further demonstrate that the formed bonds of Cu-O and Pd-O between PdCu-TiO$_2$ and C$_9$H$_9$NO$_6$ * can effectively facilitate the electron transfer (Fig. 5i-l) under light irradiation. Thereinto, the yellow area represents the electrons enrichment while the light blue represents electrons deficiency. The number of electrons transfer of PdCu (1.17 e) in PdCu-TiO$_2$ hybrids to C$_9$H$_9$NO$_6$ * -O is more than those of Pd (0.4 e) in Pd-TiO$_2$, Cu (0.64 e) in Cu-TiO$_2$ and TiO$_2$ (0.26 e), suggesting that alloying effect results in a stronger covalent character. Specifically, the excited TiO$_2$ generates electron-hole pairs under light irradiation, which are transferred to PdCu alloy by Schottky junction. Furthermore, using the paired Pd-Cu
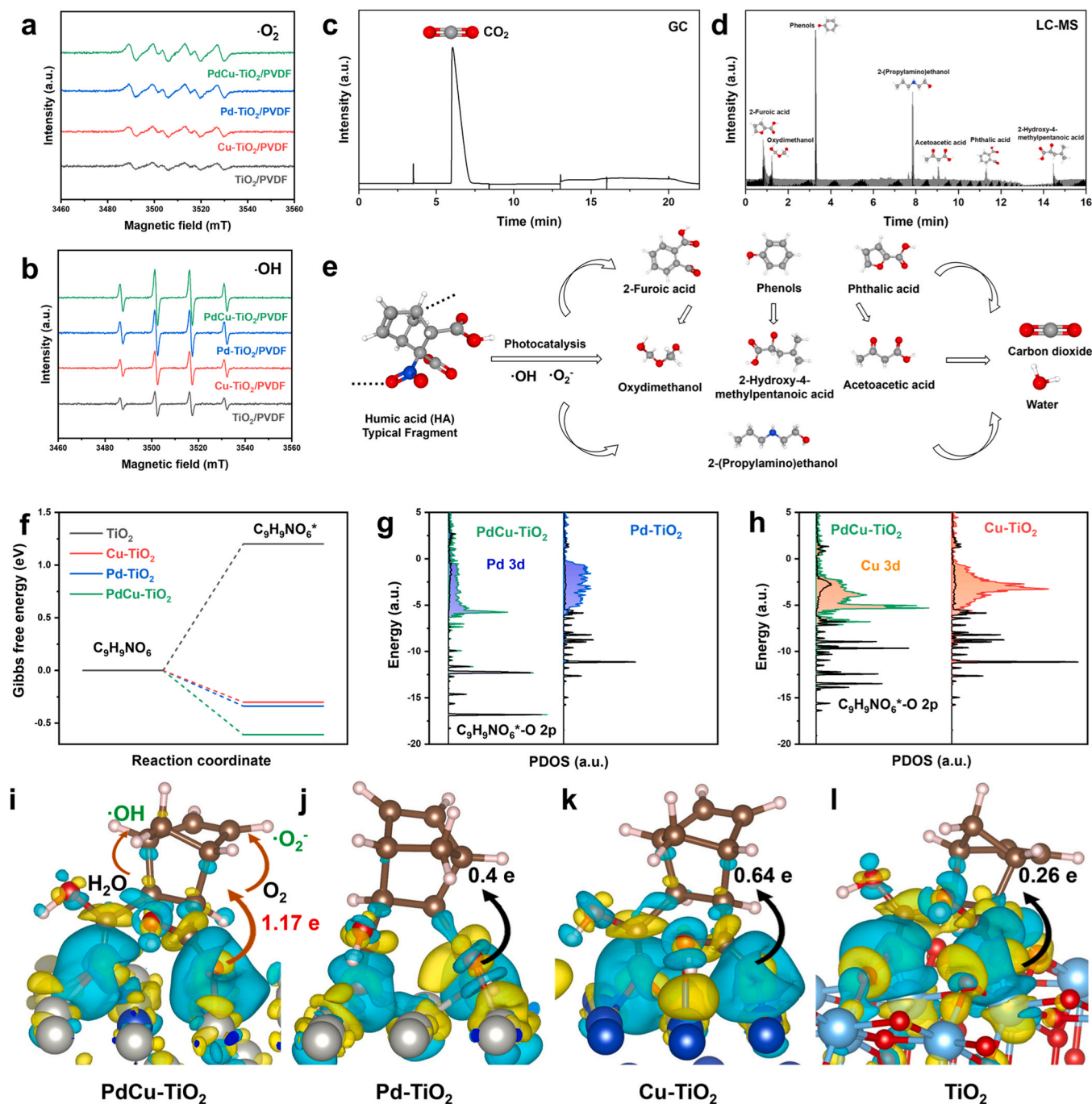
Fig. 5. ESR spectra of (a)·O$_2^-$ (trapped by DMPO in methanol), (b)·OH radical (trapped by DMPO in water) of PdCu-TiO$_2$/PVDF, Pd-TiO$_2$/PVDF, Cu-TiO$_2$/PVDF and TiO$_2$/PVDF membranes. (c) GC and (d) LC-MS chromatograms of HA degradation products after photocatalytic degradation. (e) Plausible degradation pathways for photocatalytic oxidation of HA. (f) The adsorption energy of C$_9$H$_9$NO$_6$ molecules with PdCu-TiO$_2$, Pd-TiO$_2$, Cu-TiO$_2$ and TiO$_2$. (g) Projected density of states (PDOS) plots of PdCu-TiO$_2$ and Pd-TiO$_2$. (h) Projected density of states (PDOS) plots of PdCu-TiO$_2$ and Cu-TiO$_2$. Charge density difference and corresponding charge transfer on (i) PdCu-TiO$_2$, (j) Pd-TiO$_2$, (k) Cu-TiO$_2$ and (l) TiO$_2$.

sites of PdCu alloy as springboards, electrons can be easily transferred from Pd and Cu of the paired Pd-Cu sites to C$_9$H$_9$NO$_6$ *, which further generate radical species by reacting with H$_2$O/O$_2$ for better removing HA.

4. Conclusion

As a typical representative of natural organic matter in natural waters, the removal of HA has been deemed as an urgent scientific problem. We develop a photocatalytic membrane reactor system based on PdCu-

TiO$_2$/PVDF membrane, which achieves a considerable performance in HA removal and membrane fouling alleviation. Detailed characterizations demonstrate that alloying effect of PdCu-TiO$_2$ plays multiple roles in improving PMR performance. That is, alloy effect induced electrons transfer from TiO$_2$ to PdCu alloy avoids electron-hole recombination and improves photocatalytic HA removal and anti-fouling performance of membrane; alloy effect induced photothermal effect enhances membrane permeation. Furthermore, DFT calculations prove the paired Pd-Cu sites of PdCu alloy as springboards can facilitate photo-generated electrons transfer (TiO$_2$ → Pd-Cu sites → HA), which further generate

radical species ($\cdot O_2^-$ and$\cdot OH$) by reacting with H_2O/O_2 for better HA removal. This process appears to be an excellent example of PMR systems being able to remove a priority contaminant at high permeability with good anti-fouling performance.

CRediT authorship contribution statement

Haibo Yin, Junyang Zhang and Yunlong Wang contributed equally to this work. Haibo Yin, Junyang Zhang and Yunlong Wang proposed, designed and performed the experiments, and analyzed data. All authors discussed, commented on and revised the manuscript.

Declaration of Competing Interest

The authors declare that they have no known competing financial interests or personal relationships that could have appeared to influence the work reported in this paper.

Data Availability

Data will be made available on request.

Acknowledgments

Associated Content

Supplementary data associated with this article can be found in the online version at DOI: XXXX.

Notes

The authors declare no competing financial interest.

Appendix A. Supporting information

Supplementary data associated with this article can be found in the online version at doi:10.1016/j.apcatb.2023.123085.

References

[1] J.P. Hassett, Dissolved natural organic matter as a microreactor, Science 311 (2006) 1723–1724, https://doi.org/10.1126/science.1123389.

[2] A.D. Cohen, Summit briefs policy-makers on drinking water safety, Science 368 (2020) 379–380, https://doi.org/10.1126/science.368.6489.379.

[3] A.C. Johnson, X. Jin, N. Nakada, J.P. Sumpter, Learning from the past and considering the future of chemicals in the environment, Science 367 (2020) 384–387, https://doi.org/10.1126/science.aay6637.

[4] A. Burges, H.M. Hurst, S.B. Walkden, F.M. Dean, M. Hirst, Nature of Humic Acids, Nature 199 (1963) 696–697, https://doi.org/10.1038/199696a0.

[5] X. Wu, P. Liu, Z. Gong, H. Wang, H. Huang, Y. Shi, X. Zhao, S. Gao, Humic acid and fulvic acid hinder long-term weathering of microplastics in lake water, Environ. Sci. Technol. 55 (2021) 15810–15820, https://doi.org/10.1021/acs.est.1c04501.

[6] A.M. Fankhauser, M. Bourque, J. Almazan, D. Marin, L. Fernandez, R. Hutheesing, N. Ferdousi, W.G. Tsui, V.F. McNeill, Impact of environmental conditions on secondary organic aerosol production from photosensitized humic acid, Environ. Sci. Technol. 54 (2020) 5385–5390, https://doi.org/10.1021/acs.est.9b07485.

[7] Y. Wei, H. Chu, B. Dong, X. Li, Evaluation of humic acid removal by a flat submerged membrane photoreactor, Chin. Sci. Bull. 56 (2011) 3437–3444, https://doi.org/10.1007/s11434-011-4712-8.

[8] C. Trellu, Y. Péchaud, N. Oturan, E. Mousset, D. Huguenot, E.D. van Hullebusch, G. Esposito, M.A. Oturan, Comparative study on the removal of humic acids from drinking water by anodic oxidation and electro-Fenton processes: Mineralization efficiency and modelling, Appl. Catal., B 194 (2016) 32–41, https://doi.org/10.1016/j.apcatb.2016.04.039.

[9] J. Song, P. Jin, X. Jin, X.C. Wang, Synergistic effects of various in situ hydrolyzed aluminum species for the removal of humic acid, Water Res. 148 (2019) 106–114, https://doi.org/10.1016/j.watres.2018.10.039.

[10] J. Ryu, J. Jung, K. Park, W. Song, B. Choi, J. Kweon, Humic acid removal and microbial community function in membrane bioreactor, J. Hazard. Mater. 417 (2021) 126088, https://doi.org/10.1016/j.jhazmat.2021.126088.

[11] D. Schwartz, L. Asfeld, Structure of carboxyl groups in humic acids, Nature 200 (1963) 569–570, https://doi.org/10.1038/200569a0.

[12] S.A. Visser, Oxidation-reduction potentials and capillary activities of humic acids, 581-581, Nature 204 (1964), https://doi.org/10.1038/204581a0.

[13] J. Lowe, M.M. Hossain, Application of ultrafiltration membranes for removal of humic acid from drinking water, Desalination 218 (2008) 343–354, https://doi.org/10.1016/j.desal.2007.02.030.

[14] W. Yuan, A.L. Zydney, Humic acid fouling during ultrafiltration, Environ. Sci. Technol. 34 (2000) 5043–5050, https://doi.org/10.1021/es0012366.

[15] W. Chen, C. Qian, K.-G. Zhou, H.-Q. Yu, Molecular spectroscopic characterization of membrane fouling: a critical review, Chem 4 (2018) 1492–1509, https://doi.org/10.1016/j.chempr.2018.03.011.

[16] Y. Zhao, Y. Gu, B. Liu, Y. Yan, C. Shan, J. Guo, S. Zhang, C.D. Vecitis, G. Gao, Pulsed hydraulic-pressure-responsive self-cleaning membrane, Nature 608 (2022) 69–73, https://doi.org/10.1038/s41586-022-04942-4.

[17] H. Ennaceri, K. Fischer, A. Schulze, N.R. Moheimani, Membrane fouling control for sustainable microalgal biodiesel production: a review, Renew. Sustain. Energy Rev. 161 (2022), 112335, https://doi.org/10.1016/j.rser.2022.112335.

[18] W. Zhang, L. Ding, J. Luo, M.Y. Jaffrin, B. Tang, Membrane fouling in photocatalytic membrane reactors (PMRs) for water and wastewater treatment: a critical review, Chem. Eng. J. 302 (2016) 446–458, https://doi.org/10.1016/j.cej.2016.05.071.

[19] H. Zhang, Y. Wan, J. Luo, S.B. Darling, Drawing on membrane photocatalysis for fouling mitigation, ACS Appl. Mater. Interfaces 13 (2021) 14844–14865, https://doi.org/10.1021/acsami.1c01131.

[20] C. Li, W. Sun, Z. Lu, X. Ao, S. Li, Z. Wang, F. Qi, O. Ismailova, Contribution of filtration and photocatalysis to DOM removal and fouling mechanism during in-situ UV-LED photocatalytic ceramic membrane process, Water Res. 226 (2022), 119298, https://doi.org/10.1016/j.watres.2022.119298.

[21] S. Lotfi, K. Fischer, A. Schulze, A.I. Schäfer, Photocatalytic degradation of steroid hormone micropollutants by TiO$_2$-coated polyethersulfone membranes in a continuous flow-through process, Nat. Nanotechnol. 17 (2022) 417–423, https://doi.org/10.1038/s41565-022-01074-8.

[22] L. Giorno, Membranes that filter and destroy pollutants, Nat. Nanotechnol. 17 (2022) 334–335, https://doi.org/10.1038/s41565-021-01064-2.

[23] R. Lyubimenko, O.I. Gutierrez Cardenas, A. Turshatov, B.S. Richards, A.I. Schäfer, Photodegradation of steroid-hormone micropollutants in a flow-through membrane reactor coated with Pd(II)-porphyrin, Appl. Catal., B 291 (2021), 120097, https://doi.org/10.1016/j.apcatb.2021.120097.

[24] S. Mozia, M. Tomaszewska, A.W. Morawski, A new photocatalytic membrane reactor (PMR) for removal of azo-dye Acid Red 18 from water, Appl. Catal. B 59 (2005) 131–137, https://doi.org/10.1016/j.apcatb.2005.01.011.

[25] M. Hatat-Fraile, R. Liang, M.J. Arlos, R.X. He, P. Peng, M.R. Servos, Y.N. Zhou, Concurrent photocatalytic and filtration processes using doped TiO$_2$ coated quartz fiber membranes in a photocatalytic membrane reactor, Chem. Eng. J. 330 (2017) 531–540, https://doi.org/10.1016/j.cej.2017.07.141.

[26] S. Mozia, A.W. Morawski, M. Toyoda, M. Inagaki, Application of anatase-phase TiO$_2$ for decomposition of azo dye in a photocatalytic membrane reactor, Desalination 241 (2009) 97–105, https://doi.org/10.1016/j.desal.2007.12.048.

[27] J. De Bellis, H. Petersen, J. Ternieden, N. Pfänder, C. Weidenthaler, F. Schüth, Direct dry synthesis of supported bimetallic catalysts: a study on comminution and alloying of metal nanoparticles, Angew. Chem. Int. Ed. 61 (2022), e202208016, https://doi.org/10.1002/anie.202208016.

[28] J. Ye, C. Wang, C. Gao, T. Fu, C. Yang, G. Ren, J. Lü, S. Zhou, Y. Xiong, Solar-driven methanogenesis with ultrahigh selectivity by turning down H$_2$ production at biotic-abiotic interface, Nat. Commun. 13 (2022) 6612, https://doi.org/10.1038/s41467-022-34423-1.

[29] G. Jia, Y. Pang, J. Ning, U. Banin, B. Ji, Heavy-metal-free colloidal semiconductor nanorods: recent advances and future perspectives, Adv. Mater. 31 (2019) 1900781, https://doi.org/10.1002/adma.201900781.

[30] Y. Xin, S. Li, Y. Qian, W. Zhu, H. Yuan, P. Jiang, R. Guo, L. Wang, High-entropy alloys as a platform for catalysis: progress, challenges, and opportunities, ACS Catal. 10 (2020) 11280–11306, https://doi.org/10.1021/acscatal.0c03617.

[31] M. Zhou, C. Li, J. Fang, Noble-metal based random alloy and intermetallic nanocrystals: syntheses and applications, Chem. Rev. 121 (2021) 736–795, https://doi.org/10.1021/acs.chemrev.0c00436.

[32] J.Q. He, D.Y. Chen, N.J. Li, Q.F. Xu, H. Li, J.H. He, J.M. Lu, Controlled fabrication of mesoporous ZSM-5 zeolite-supported PdCu alloy nanoparticles for complete oxidation of toluene, Appl. Catal. B-Environ. 265 (2020), https://doi.org/10.1016/j.apcatb.2019.118560.

[33] V.S. Marakatti, S.C. Sarma, B. Joseph, D. Banerjee, S.C. Peter, Synthetically tuned atomic ordering in PdCu nanoparticles with enhanced catalytic activity toward solvent-free benzylamine oxidation, ACS Appl. Mater. Interfaces 9 (2017) 3602–3615, https://doi.org/10.1021/acsami.6b12253.

[34] B. Wang, Y.Y. Wang, J.Z. Li, X.N. Guo, G.L. Bai, X.L. Tong, G.Q. Jin, X.Y. Guo, Photocatalytic Sonogashira reaction over silicon carbide supported Pd-Cu alloy nanoparticles under visible light irradiation, Catal. Sci. Technol. 8 (2018) 3357–3362, https://doi.org/10.1039/C8CY00618K.

[35] X.T. Cai, A. Wang, J.W. Wang, R.X. Wang, S.X. Zhong, Y.L. Zhao, L.J. Wu, J. R. Chen, S. Bai, Order engineering on the lattice of intermetallic PdCu co-catalysts

for boosting the photocatalytic conversion of CO_2 into CH_4, J. Mater. Chem. A 6 (2018) 17444–17456, https://doi.org/10.1039/C8TA06204H.

[36] R. Long, Y. Li, Y. Liu, S. Chen, X. Zheng, C. Gao, C. He, N. Chen, Z. Qi, L. Song, J. Jiang, J. Zhu, Y. Xiong, Isolation of Cu atoms in Pd lattice: forming highly selective sites for photocatalytic conversion of CO_2 to CH_4, J. Am. Chem. Soc. 139 (2017) 4486–4492, https://doi.org/10.1021/jacs.7b00452.

[37] F. Wang, Z. Zhang, I. Shakir, C. Yu, Y. Xu, 2D polymer nanosheets for membrane separation, Adv. Sci. 9 (2022) 2103814, https://doi.org/10.1002/advs.202103814.

[38] C. Li, J. Yang, L. Zhang, S. Li, Y. Yuan, X. Xiao, X. Fan, C. Song, Carbon-based membrane materials and applications in water and wastewater treatment: a review, Environ. Chem. Lett. 19 (2021) 1457–1475, https://doi.org/10.1007/s10311-020-01112-8.

[39] G. Liu, W. Jin, Pervaporation membrane materials: recent trends and perspectives, J. Membr. Sci. 636 (2021), 119557, https://doi.org/10.1016/j.memsci.2021.119557.

[40] F. Liu, N.A. Hashim, Y. Liu, M.R.M. Abed, K. Li, Progress in the production and modification of PVDF membranes, J. Membr. Sci. 375 (2011) 1–27, ⟨https://doi.org/10.1016/j.memsci.2011.03.014⟩.

[41] L. Lu, W. Ding, J. Liu, B. Yang, Flexible PVDF based piezoelectric nanogenerators, Nano Energy 78 (2020), 105251, https://doi.org/10.1016/j.nanoen.2020.105251.

[42] I. Kriegel, F. Scotognella, L. Manna, Plasmonic doped semiconductor nanocrystals: Properties, fabrication, applications and perspectives, Phys. Rep. -Rev. Sec. Phys. Lett. 674 (2017) 1–52, https://doi.org/10.1016/j.physrep.2017.01.003.

[43] L. Zhou, D.F. Swearer, C. Zhang, H. Robatjazi, H. Zhao, L. Henderson, L. Dong, P. Christopher, E.A. Carter, P. Nordlander, N.J. Halas, Quantifying hot carrier and thermal contributions in plasmonic photocatalysis, Science 362 (2018) 69–72, https://doi.org/10.1126/science.aat6967.

[44] M.-Q. Yang, M. Gao, M. Hong, G.W. Ho, Visible-to-NIR photon harvesting: progressive engineering of catalysts for solar-powered environmental purification and fuel production, Adv. Mater. 30 (2018) 1802894, https://doi.org/10.1002/adma.201802894.

[45] Y.-S. Jun, X. Wu, D. Ghim, Q. Jiang, S. Cao, S. Singamaneni, Photothermal membrane water treatment for two worlds, Acc. Chem. Res. 52 (2019) 1215–1225, https://doi.org/10.1021/acs.accounts.9b00012.

[46] S. Santoro, A.H. Avci, A. Politano, E. Curcio, The advent of thermoplasmonic membrane distillation, Chem. Soc. Rev. 51 (2022) 6087–6125, https://doi.org/10.1039/D0CS00097C.

[47] T. Uekert, C.M. Pichler, T. Schubert, E. Reisner, Solar-driven reforming of solid waste for a sustainable future, Nat. Sustain. 4 (2021) 383–391, https://doi.org/10.1038/s41893-020-00650-x.

[48] I. Jeon, E.C. Ryberg, P.J.J. Alvarez, J.H. Kim, Technology assessment of solar disinfection for drinking water treatment, Nat. Sustain. 5 (2022) 801–808, https://doi.org/10.1038/s41893-022-00915-7.

[49] H. Yin, J. Li, New insight into photocatalytic CO_2 conversion with nearly 100% CO selectivity by CuO-Pd/$H_xMoO_{3−y}$ hybrids, Appl. Catal., B 320 (2023), 121927, https://doi.org/10.1016/j.apcatb.2022.121927.

[50] H. Yin, Z. Chen, S. Xiong, J. Chen, C. Wang, R. Wang, Y. Kuwahara, J. Luo, H. Yamashita, Y. Peng, J. Li, Alloying effect-induced electron polarization drives nitrate electroreduction to ammonia, Chem. Catal. 1 (2021) 1088–1103, https://doi.org/10.1016/j.checat.2021.08.014.

[51] B. Yin, Z. Qiao, C. Liu, Microscopic mechanisms of fluid flow at solid/liquid interfaces and their implications for anti-fouling surfaces, Mater. Des. 106 (2016) 226–234, https://doi.org/10.1016/j.matdes.2016.05.116.